Technical University of Denmark

DTU

An all-fiber image-reject homodyne coherent Doppler wind lidar

Foroughi Abari, Farzad; Pedersen, Anders Tegtmeier; Mann, Jakob

DTU Library
Technical Information Center of Denmark

An all-fiber image-reject homodyne coherent Doppler wind lidar

Cyrus F. Abari,[*] **Anders T. Pedersen, and Jakob Mann**

Department of Wind Energy, Technical University of Denmark, Roskilde DK-4000, Denmark
[*]*cyrus.abari@gmail.com*

Abstract: In this paper, we present an alternative approach to the down-conversion (translation) of the received optical signals collected by the antenna of an all-fiber coherent Doppler lidar (CDL). The proposed method, widely known as image-reject, quadrature detection, or in-phase/quadrature-phase detection, utilizes the advances in fiber optic communications such that the received signal can be optically down-converted into baseband where not only the radial velocity but also the direction of the movement can be inferred. In addition, we show that by performing a cross-spectral analysis, enabled by the presence of two independent signal observations with uncorrelated noise, various noise sources can be suppressed and a more simplified velocity estimation algorithm can be employed in the spectral domain. Other benefits of this architecture include, but are not limited to, a more reliable measurement of radial velocities close to zero and an improved bandwidth. The claims are verified through laboratory implementation of a continuous wave CDL, where measurements both on a hard and diffuse target have been performed and analyzed.

OCIS codes: (280.3640) Lidar; (010.3640) Lidar; (120.4640) Optical instruments.

References and links

1. G. Fiocco and L. D. Smullin, "Detection of scattering layers in the upper atmosphere (60-140 km) by optical radar," Nature (London) **199**(1), 1275–1276 (1963).
2. A. V. Jelalian, *Laser radar systems* (Boston Artech, 1992).
3. ZephIR 300 technical specifications, (ZephIR Lidar, 2014). http://www.zephirlidar.com/resources/technical-specs.
4. WINDCUBE V2, a 200m vertical wind Doppler lidar, (Leosphere, 2014). http://www.leosphere.com/products/vertical-profiling/windcube-v2.
5. WINDAR functional specifications, (WINDAR PHOTONICS, 2014). http://www.windarphotonics.com/product.
6. F. Bingöl, J. Mann, and D. Foussekis, "Conically scanning lidar error in complex terrain," Meteorologische Zeitschrift **18**(2), 189–195 (2009).
7. S. Lang and E. McKeogh, "Lidar and sodar measurements of wind speed and direction in upland terrain for wind energy purposes," Remote Sens. **3**(9), 1871–1901 (2011).
8. T. Mikkelsen, N. Angelou, K. Hansen, M. Sjöholm, M. Harris, C. Slinger, P. Hadley, R. Scullion, G. Ellis, and G. Vives, "A spinner-integrated wind lidar for enhanced wind turbine control," Wind Energy **16**(4), 625–643 (2013).
9. D. Schlipf, D. J. Schlipf, and M. Kühn, "Nonlinear model predictive control of wind turbines using lidar," Wind Eng. **16**(7), 1107–1129 (2012).
10. I. Antoniou, S. M. Pedersen, and P. B. Enevoldsen, "Wind shear and uncertainties in power curve measurement and wind resources," Wind Eng. **33**(5), 449–468 (2010).
11. C. J. Karlsson, F. A. Olsson, D. Letalick, and M. Harris, "All-fiber multifunction continuous-wave coherent laser radar at 1.55 μm for range, speed, vibration, and wind measurements," Appl. Opt. **39**(21), 3716–3726 (2000).
12. G. N. Pearson, P. J. Roberts, J. R. Eacock, and M. Harris, "Analysis of the performance of a coherent pulsed fiber lidar for aerosol backscatter applications," Appl. Opt. **41**(30), 6442–6450 (2002).

13. P. Lindelöw, "Fiber based coherent lidars for remote wind sensing," PhD dissertation, Dept. of Photon. Eng., Tech. Univ. of Denmark, Lyngby, Denmark, 2007.

14. S. F. Jacobs, "Optical heterodyne (coherent) detection," Am. J. Phys. **56**(3), 235–245 (1988).

15. O. E. DeLange, "Optical heterodyne detection," IEEE Spectrosc. **5**(10), 77–85 (1968).

16. B. Razavi, "Design considerations for direct-conversion receivers," IEEE Trans. Circuits Syst. II: Analog Digit. Signal Process. **44**(6), 428–435 (1997).

17. L. Richter, H. Mandelberg, M. Kruger, and P. McGrath, "Linewidth determination from self-heterodyne measurements with subcoherence delay times," IEEE J. Quantum Electron. **22**(11), 2070–2074 (1986).

18. M. Harris, G. N. Pearson, K. D. Ridley, C. J. Karlsson, F. A. Olsson, and D. Letalick "Single-particle laser Doppler anemometry at 1.5 μm," Appl. Opt. **40**(6), 969–973 (2001).

19. J. R. Barry and E. A. Lee, "Performance of coherent optical receivers," Proc. IEEE **78**(8), 1369–1394 (1990).

20. A. Valle and L. Pesquera, "Relative intensity noise of multitransverse-mode vertical-cavity surface-emitting lasers," IEEE Photon. Technol. Lett. **13**(4), 272–274 (2001).

21. R. Stierlin, R. Bättig, P. D. Henchoz, and H. P. Weber, "Excess-noise suppression in a fiber-optic balanced heterodyne detection system," Opt. Quantum Electron. **18**(6), 445–454 (1986).

22. L. Ma, Y. Hu, S. Xiong, Z. Meng, and Z. Hu, "Intensity noise and relaxation oscillation of a fiberlaser sensor array integrated in a single fiber," Opt. Lett. **35**(1), 1795–1797 (2010).

23. G. A. Cranch, M. A. Englund, and C. K. Kirkendal, "Intensity noise characteristics of erbium-doped distributed-feedback lasers," IEEE J. Quantum Electron. **39**(12), 1579–1587 (2003).

24. A. D. McCoy, L. B. Fu, M. Ibsen, B. C. Thomsen, and D. J. Richardson, "Relaxation oscillation noise suppression in fiber DFB lasers using a semiconductor optical amplifier," in Conference on Lasers and Electro-Optics, 2004 OSA CLEO Poster Session II (Optical Society of America, 2004), page CWA56.

25. P. J. Rodrigo and C. Pedersen. "Comparative study of the performance of semiconductor laser based coherent Doppler lidars," Proc. SPIE **8241**, 824112 (2012).

26. B. J. Rye and R. M. Hardesty, "Discrete spectral peak estimation in incoherent backscatter heterodyne lidar. I: Spectral accumulation and the Cramer-Rao lower bound," IEEE Trans. Geosci. Remote Sens. **31**(1), 16–27 (1993).

27. J. M. B. Dias and J. M. N. Leitão, "Nonparametric estimation of mean Doppler and spectral width," IEEE Trans. Geosci. Remote Sens. **38**(1), 271–282 (2000).

28. M. H. Hayes, *Statistical Digital Signal Processing and Modeling* (John Wiley & Sons, 1996).

29. A. T. Pedersen, C. F. Abari, J. Mann, and T. Mikkelsen, "Theoretical and experimental signal-to-noise ratio assessment in new direction sensing continuous-wave Doppler lidar," in J. Phys.: Conf. Ser., Vol. 524 (IOP Publishing, 2014), paper 012004.

30. M. Harris, G. N. Pearson, J. M. Vaughan, and D. Letalick, "The role of laser coherence length in continuous-wave coherent laser radar," J. Mod. Opt. **45**(8), 1567–1581 (2009).

31. B. Moslehi, "Analysis of optical phase noise in fiber-optic systems employing a laser source with arbitrary coherence time," J. Lightw. Technol. **4**(9), 1334–1351 (1986).

32. C. A. Hill, M. Harris, and K. D. Ridley, "Fiber-based 1.5 μm lidar vibrometer in pulsed and continuous modes," Appl. Opt. **46**(20), 4376–4385 (2007).

33. C. Allen, Y. Cobanoglu, S. K. Chong, and S. Gogineni, "Development of a 1310-nm, coherent laser radar with RF pulse compression," in Proceedings of IEEE Geoscience and Remote Sensing Symposium (IEEE, 2000), pp. 1784–1786.

34. L. G. Kazovsky, L. Curtis, W. C. Young, and N. K. Cheung, "All-fiber 90° optical hybrid for coherent communications," Appl. Opt. **26**(3), 437–439 (1987).

35. D. O. Hogenboom and C. A. DiMarzio, "Quadrature detection of a Doppler signal," Appl. Opt. **37**(13), 2569–2572 (1998).

36. N. Angelou, C. F. Abari, J. Mann, T. Mikkelsen, and M. Sjöholm, "Challenges in noise removal from Doppler spectra acquired by a continuous-wave lidar," Presented at the 26th International Laser Radar Conference, Porto Heli, Greece, 25-29 June 2012.

1. Introduction

Light detection and ranging (lidar) instruments have been in use for remote sensing of atmospheric conditions, including the atmospheric boundary layer (ABL), for about five decades. For instance, Fiocco and Smullin [1] demonstrated one of the early application of lidars (also known as optical radar) in atmospheric characterizations and meteorological observations. Wind lidars were already employed in early 1970s [2]. Following advances in fiber optic communications, where lasers with wavelengths close to 1550 nm are used, this technology has been extensively used in all-fiber CDLs. Commercial examples of such systems are widely available: for instance, ZephIR from ZephIR Lidar [3], Windcube from Leosphere [4], and WindEye from

WINDAR Photonics [5] are examples of all-fiber CDLs. The all-fiber 1550 nm CDLs have a master oscillator power amplifier architecture (MOPA) where a compact laser source, known as the master oscillator (MO), is utilized for the generation of a highly coherent light. Examples of MOs are distributed feedback (DFB) fiber or semiconductor lasers. DFB lasers have a small form factor and provide high sensitivity, robustness, and low levels of phase noise. The fiber optic technology, used in optical communications industry, is employed for the generation, amplification, transmission, and manipulation of the laser beam in all-fiber CDLs. Applications of CDLs in the wind industry cover, but are not limited to, the measurement of wind velocities in terrain for the characterization and optimization of wind turbine installation (wind resource assessment) [6, 7], the measurement of the incoming wind flow for optimal wind turbine yaw and pitch control [8, 9], and power curve verification [10].

Typically, there are two major variants of mono-static CDLs used for wind measurements, i.e., continuous wave (CW) and pulsed. In CW CDLs ranging is achieved by translating the end facet of the delivery fiber along the optical axis of the telescope [11]. Thus, ranging is achieved by focusing the laser beam on the range of interest. On the other hand, pulsed lidars emit a laser pulse for wind flow characterizations [12]. In such systems, ranging is achieved by range gating the received signals, i.e., the collected scattering from aerosol particles [13]. In both types of systems, the backscatter from aerosol particles are collected through a telescope which passes them on to the following stages for further processing.

Due to numerous advantages provided by digital signal processing algorithms, the detected signals are typically digitized for further treatment. However, the available analog-to-digital converters (A/D) have limited bandwidth (BW) that is far below the laser frequency, conventionally known as the carrier frequency. Besides, the opto-electronic components, such as photodetectors have limited BW and cannot follow signal fluctuations in the THz region. As a result, it is imperative to down-convert the optical signals into lower radio frequency (RF) spectrum known as intermediate frequency (IF) or baseband, also known as zero-IF. Coherent receivers achieve this by mixing (beating) the reflections with a local oscillator (LO) signal, usually derived from the MO. Depending on the LO frequency and the front-end treatment of the signals, various architectures may be realized. In fact, the optical coherent detection is "simply an extension into the optical region, of a well-known radio-frequency technique used in superheterodyne receiver". [14]

Depending on the frequency where the optical signal is translated [15] the architectures in CDLs may be categorized into two main classes: direct-conversion (homodyne) and heterodyne architectures. In homodyne receivers, the LO and signal carrier frequencies are equal. In heterodyne receivers, the carrier frequency is different from the LO's. A homodyne or heterodyne receiver may be realized through either real mixing or in-phase/quadrature-phase (I/Q) mixing, also known as complex mixing. The complex mixing process is also known as the image-reject or quadrature mixing principle. The inability to perform an image rejection (and thus real mixing) in telecommunications results in possible corruption of the transmitted information because the two sides of the band overlap and interfere [16]. In CDLs it results in a symmetric spectrum where the sign of the radial wind velocity cannot be discriminated which is a rather serious issue for certain applications. To solve the sign ambiguity, a few receiver architectures can be employed, the most popular of which are heterodyne receivers with IF sampling and homodyne receivers with complex mixing. Heterodyne mixing with IF sampling is a well-known and widely used approach for signal detection in CDLs.

In this paper, we show that by employing a direct image-reject architecture in a CW CDL, made feasible through commercially available components for optical communications, a more robust and accurate CDL can be prototyped. The result is a system that has twice the BW as existing CDLs that employ heterodyning with IF sampling for a similar system configuration. In

addition, the prototype system provides a better estimate of radial velocities close to zero where the signal is contaminated by noise in heterodyne receivers. Furthermore, it is shown that by performing a cross-spectral analysis between the in-phase and quadrature-phase components, the noise sources (mainly the shot noise) can be suppressed and a less signal processing intensive algorithm employed to extract the radial velocity information. Although the focus of the paper is on CW CDLs many of the principles can be applied to a pulsed CDL with no or minor modifications.

The paper is divided into several sections. In Section 2, we adopt a simple but efficient signal model associated with coherent detection in an all-fiber homodyne CW CDL with real mixing to present the concepts and lay a mathematical framework. In Section 3, we present the image-reject homodyne receiver and analyze its theoretical performance with respect to receivers with real mixing such as the one described in Section 2. A laboratory prototype of an all-fiber image-reject homodyne CW CDL, as described in this paper, is presented in Section 4 where a few measurement results on hard and diffused target are presented as a proof of concept. Throughout the paper, an effort has been made to emphasize the most important parameters affecting the CDL performance for the discussed architectures. Meanwhile, wherever deemed appropriate, we have ignored the topics secondary to the results presented in this paper. We have also adopted a number of simplifications without sacrificing the generality and applicability of the results. The optical and electronic components in this paper are assumed to be lossless and ideal unless otherwise specified in the text.

2. Coherent detection and signal modeling

Before analyzing the image-reject receiver architectures, it is worthwhile to adopt appropriate transmit and receive signal models associated with a CW CDL in a MOPA configuration. Fig. 1 illustrates one of the simplest receiver architectures adopted for such systems. In this system, the laser source signal, MO, is modeled after the fundamental mode of an optical resonator, i.e., TEM_{00} [15], where the transverse irradiance has a Gaussian distribution and the longitudinal intensity is Lorentzian. Irrespective of the temporal irradiance shape associated with the transmitted laser signal, we can adopt the following mathematical model in time domain for the electric field fluctuations of the optical signal at the output of the erbium doped fiber amplifier (EDFA):

$$L(t) = \sqrt{2p}\cos\left[2\pi f_c t + \theta(t)\right] + L_R(t), \tag{1}$$

where p is the optical signal power, f_c is the laser frequency (also known as the carrier frequency), $\theta(t)$ is the laser phase noise that defines the laser line width [17], and $L_R(t)$ is the relative intensity noise (RIN) of the laser. After passing through the optical circulator, $L(t)$ is split into a transmit signal $s(t)$ and LO signal $L_O(t)$. LO in this particular system configuration is derived by collecting the back reflections from the end facet of the delivery fiber, i.e., the fiber at the input of the telescope. The LO power can be adjusted by polishing the end facet of the delivery fiber [11] at the desired angle. Thus, the transmitted signal, $s(t)$, through the telescope is a major fraction of $L(t)$ where $s(t) = \sqrt{1-\varepsilon}L(t)$. Furthermore, $0 < \varepsilon < 1$ is the splitting ratio that controls the LO power. For reflections from a diffuse target such as backscatter from aerosol particles in the air the received signal for the collected light by the telescope can be modeled as

$$r(t) = \left[2(1-\varepsilon)p\right]^{1/2}\sum_{l=0}^{L-1}\alpha_l\cos\left[2\pi(f_c+\Delta f_l)t + \theta(t) + \phi_l\right], \tag{2}$$

where α_l is the net optical attenuation , Δf_l is the Doppler shift due to motion, ϕ_l is the phase factor associated with the lth aerosol particle, and L is the number of aerosol particles in the measurement volume. Furthermore, α_l, Δf_l, and ϕ_l can be modeled as independent random
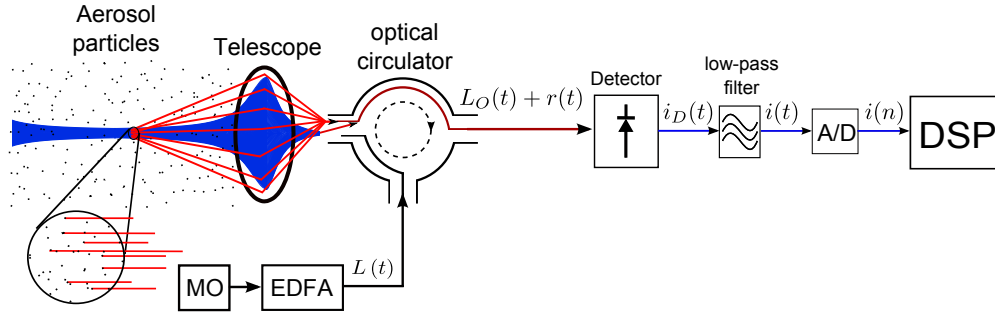
Fig. 1: Homodyne receiver with real mixing. The LO is derived from the Fresnel reflections at the end facet of delivery fiber at the output of the circulator.

variables where Δf_l has a Gaussian distribution and ϕ_l is a uniformly distributed random variable with $\phi_l \in [0, 2\pi)$. In Eq. (2) the effect of $L_R(t)$ in the collected signal has been ignored because its power is insignificant compared to the power of the transmitted signal. Moreover, the average received power in Eq. (2) is approximated by [18]

$$p_r = \pi p_t \beta(\pi) \lambda, \tag{3}$$

where $p_t = (1 - \varepsilon)p$ is the transmit signal power, $\beta(\pi)$ is the atmospheric backscatter coefficient, and λ is the wavelength.

The phase noise, $\theta(t)$, is commonly characterized by a Wiener process [19]. It can be shown that phase noise exhibits a Lorentzian shaped spectrum whose 3-dB BW defines the laser linewidth, characterizing the coherence length of the laser. Phase noise in modern DFB lasers can be improved such that its detrimental effect in coherent lidars can be ignored for the majority of practical applications. Thus, for simplicity and without loss of generality, we ignore the effect of phase noise for the remainder of this paper.

On the other hand, RIN can be of practical importance, especially for DFB fiber lasers. Although, most of RIN will be buried under a detector's shot noise, the RIN peak, associated with the laser's relaxation frequency [20], may skew the measurements. This is more pronounced for gas lasers such as He-Ne [21] and fiber lasers [22] where the peak appears in the low-frequency region of the spectrum. Therefore, the presence of RIN affects the measurement results and the minimum detectable signals [23] and is a limiting factor, especially in optical remote sensing and meteorology [24]. It has been shown [25] that the RIN peak for some semiconductor lasers is outside the measurement range of interest and does not pose a problem when compared to fiber based lasers.

To illustrate the concepts in this paper, we have derived the mathematical models associated with backscatter from a single particle. The models provide a simple mathematical way to present the concepts that hold for both hard targets and diffuse targets. Verification of the results has been provided through atmospheric measurements presented in Section 4.

Following Eq. (2), the received signal associated with backscatter from a single particle can be modeled as

$$r(t) = \alpha \left[2(1 - \varepsilon)p\right]^{1/2} \cos\left[2\pi(f_c + \Delta f)t + \phi\right], \tag{4}$$

where subscript l has been dropped for a single particle.

If LO is

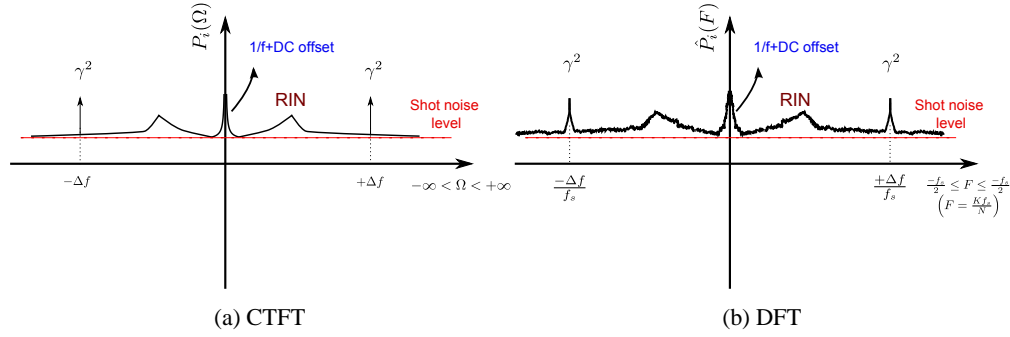$$L_O(t) = \sqrt{2\varepsilon p}\cos(2\pi f_c t), \tag{5}$$

Fig. 2: Examples of the PSD associated with the baseband signal. (a) The spectra when CTFT has been performed to estimate the spectra. (b) The effect of estimation noise when a limited observation time is available for spectral processing after digitization.

then mixture of the received and LO signals, i.e., $r(t) + L_o(t)$, is impinged on a photo detector whose response to the light intensity, in the form of an electric current, can be modeled as

$$i(t) \propto [r(t) + L_o(t)]^2. \tag{6}$$

After some mathematical manipulation and simplifications, the resultant current at the output of the low-pass filter is

$$i(t) = 2\gamma \cos[2\pi(\Delta f)t + \phi] + \eta(t), \tag{7}$$

where $\gamma = p\alpha R_D [\varepsilon(1-\varepsilon)]^{1/2}$ and $\eta(t)$ is the total noise. Furthermore, R_D is the detector responsivity and

$$\eta(t) = \eta_{dc} + \eta_R(t) + \eta_{sn}(t) + \eta_f(t), \tag{8}$$

where η_{dc} is the DC noise, $\eta_R(t)$ is the detected RIN, $\eta_{sn}(t)$ is the shot noise, and $\eta_f(t)$ is the $1/f$ noise. In Eq. (8) we have ignored the effect of thermal noise and the detector's dark noise as they are insignificant when compared to other noise sources. Furthermore, the shot noise power is

$$p_{\eta_{sn}} = 2E R_D p_{LO} B, \tag{9}$$

where $E = 1.3 \times 10^{-19}$ J is the light quantum energy, p_{LO} is the local oscillator power, and B is the BW.

The baseband signal in Eq. (7) contains the Doppler shift information which can be extracted through spectral analysis of the signal. Thus, for the received signal in Eq. (7)

$$P_i(\Omega) = \mathscr{F}\left\{ \mathbb{E}\left[i(t)\overline{i(t+\tau)} \right] \right\} = \gamma^2 \delta(\Omega - \Delta\Omega) + \gamma^2 \delta(\Omega + \Delta\Omega) + P_\eta(\Omega), \tag{10}$$

where $P_i(\Omega)$ and $P_\eta(\Omega)$ are the power spectral density (PSD) of the signal and noise respectively, $\mathscr{F}$ is the continuous-time Fourier transform (CTFT), Ω is the frequency in Laplace domain, $\mathbb{E}[\cdot]$ denotes the ensemble average operation, and $\overline{(\cdot)}$ represents the complex conjugate operation. Fig. 2(a) illustrates an example of the PSD associated with Eq. (10). As can be seen, the PSD is symmetric around zero frequency.

In practice, due to the advances in digital signal processors and computers, the signals need to be digitized for further processing. However, only a limited observation time is available for processing (e.g., spectral processing) of the digitized signal. There are various ways [26, 27] to estimate the PSD of a signal such as the one in Eq. (7). A widely used method is to estimate the

spectra through periodograms [28], which when applied to the digitized version of the signal in Eq. (7), results in

$$\hat{P}_i(K) = \frac{f_s}{M} \sum_{m=0}^{M-1} |I(K)|^2,$$ (11)

where K is the discrete frequency component, M is the number of averages, and f_s is the sampling frequency. In addition, $I(K)$ is the discrete Fourier transform (DFT) defined as

$$I(K) = \frac{1}{N} \sum_{n=0}^{N-1} i(n) \exp\left(-2\pi j \frac{n}{N} K\right),$$ (12)

where N is the number of DFT points. Compared to Eq. (10),

$$\hat{P}_i(K) = P_i(\Omega_K) + \eta_{est}(K),$$ (13)

where $\eta_{est}(K)$ is the estimation noise and $\Omega_K = \frac{K f_s}{N}$. For the shot-noise limited operational mode, where the effect of all other noise sources are neglected, $\eta_{est}(K)$ can be modeled as a Gaussian random variable [29] where

$$\mu_{\eta_{est}}(K) = \mathbb{E}\{\eta_{est}(K)\} = \eta_{sn}(\Omega_K),$$
$$\sigma_{\eta_{est}}(K) = \frac{P_i(\Omega_K)}{\sqrt{M}}.$$ (14)

Fig. 2(b) shows an example of an estimated PSD for the signal in Eq. (7).

The ability to detect the Doppler shift in practice depends on the performance of the estimation algorithm that can discriminate the signal information from the noise, especially, the estimation noise. As a result, it seems necessary to define a new quantity:

$$\text{SENR}_i = \frac{P_i(K_D) - P_\eta(K_D)}{\sigma_{\eta_{est}}(K)|_{(K \neq K_D)}},$$ (15)

where SENR_i is the signal-to-estimation-noise-ratio and $K_D = \pm \lfloor \frac{\Delta f}{f_s} \rfloor N$, the frequency associated with the Doppler peak. Please note that SENR is different from (the commonly used)

$$\text{SNR}_i = \frac{\int_{-\infty}^{+\infty} P_i(\Omega) \, d\Omega - p_\eta}{p_\eta},$$ (16)

where $p_\eta = \int_{-\infty}^{+\infty} P_\eta(\Omega) \, d\Omega$. For a shot-noise limited operation, where the effect of other noise sources and unwanted signals is ignored, and assuming a flat spectra the SNR for the presented homodyne receiver with real mixing is

$$\text{SNR}_i = \frac{\alpha^2 R_D (1-\varepsilon) p}{EB}.$$ (17)

One of the major sources of unwanted signals is the non-ideal behavior of optical components such as the optical circulator. For instance, due to the presence of phase noise and cross-talk in optical circulators the estimated signal may suffer from interferometric noise [30, 31]. Reflections from optical components such as telescope lenses can also be compounding. A thorough analysis of SENR has been performed in [29] from which it can be inferred that the SENR for the simple homodyne system, described in this section, is

$$\text{SENR}_i = \frac{\sqrt{M} \alpha^2 R_D (1-\varepsilon) p}{E} = B\sqrt{M}\text{SNR}_i.$$ (18)
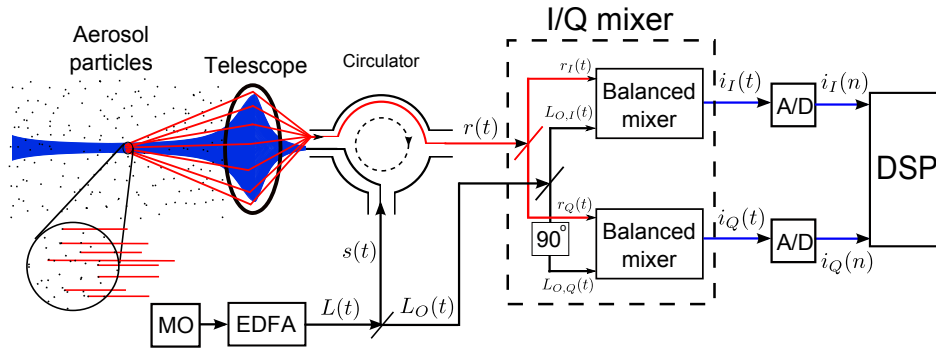
Fig. 3: The schematic of the image-reject homodyne receiver.

As shown in Eq. (16), SNR refers to the ratio of the signal power and the instrument noise power (e.g., shot-noise). In spectral analysis, however, SENR seems to be the major player in determining how well the signal can be estimated when buried in estimation noise.

Despite its many advantages, the above-modeled system suffers from an inability to discriminate the direction of travel, i.e., the sign of the radial velocity. This is evident from the example PSDs illustrated in Figs. 2(a)-2(b), in which the presence of the image component of the Doppler signal masks the sign of the radial velocity. To extract the direction of travel, other receiver architectures need to be implemented. Examples of such systems are heterodyne receivers with IF sampling [32], super heterodyne receivers [33], and image-reject homodyne receivers. In the following sections we have presented a detailed analysis of an all-fiber image-reject homodyne receiver. The presented system not only resolves the sign ambiguity, but it also benefits from a novel approach in signal processing that eliminates the major noise sources and simplifies extraction of the Doppler information from the signal. Additionally, through prototyping the system we will demonstrate its performance for a number of different measurement scenarios, including measurement on hard and diffuse targets.

3. Image-reject architecture

To resolve the ambiguity associated with the direction of travel, an image-reject homodyne receiver can be utilized. In image-reject homodyne receivers, the return signal is mixed with two realizations of the LO signal where one realization is exactly 90 degrees out of phase with respect to the other one. This concept is widely used in radio systems [16] and in optical communications [34]. The idea has also been tested as a solution in CDLs using open space optics. For instance, it has been shown [35] that by using a circularly polarized light one can attain the in-phase and quadrature-phase LO realizations required for this principle. The reported results were based on measurements on a hard target in a laboratory environment. However, to the best of our knowledge, this is the first time an all-fiber system implementation of a CDL employing an image-reject homodyne architecture has been reported in literature where measurements for both hard and diffuse targets have been successfully performed.

Fig. 3 provides an illustration of the system implementation for an all-fiber image-reject architecture. In contrast to the homodyne receiver illustrated in Fig. 1, the LO signal in this system is not derived from Fresnel reflection at the end facet of the delivery fiber at the output of the optical circulator. Instead, two realizations of the LO with equal power are obtained through an I/Q mixer. The I/Q mixer has two fundamental roles. First, it provides two realization of the LO required for in-phase and quadrature-phase components. Second, it utilizes two balanced
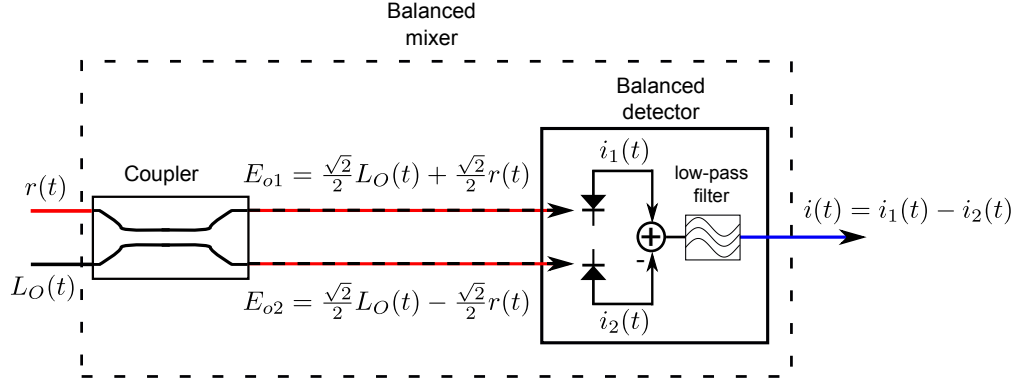
Fig. 4: The schematic of the balanced mixer. The mixer consists of a balanced coupler and two balanced photo diodes connected in reverse.

mixers to mix the return signal with the LO, detect the result, and filter the signals for delivery to the next stage for digitization and further processing. The splitters inside the I/Q mixer provide a 50/50 splitting ratio while the 90 degree phase shift is achieved through a finely tuned delay line. Thus,

$$\begin{cases} L_{O,I}(t) = \sqrt{\varepsilon p}\cos\left(2\pi f_c t\right), \\ L_{O,Q}(t) = \sqrt{\varepsilon p}\sin\left(2\pi f_c t\right). \end{cases} \tag{19}$$

Furthermore, it can be shown that, $p_{LO,I_1} = p_{LO,I_2} = p_{LO,Q_1} = p_{LO,Q_2} = \frac{\varepsilon p}{4}$, where subindices refer to the individual photo-diodes at the in-phase and quadrature-phase legs.

The balanced mixer, as shown in Fig. 4, is mainly composed of a fiber coupler and two matched photo diodes. The input signals (the return signal and the LO) fed into the coupler, having a 50-50 coupling ratio, are mixed such that the output legs provide a common and differential signal components. At the output of the matched diode pair the common component is rejected and the differential mode is passed through. For such a configuration, the common mode rejection ratio (CMRR) depends on the matching of the two photo-diodes as well as the coupling ratio. In this paper, we have assumed ideal matching between the two diodes as well as an ideal and stable 50% coupling ratio.

After some mathematical manipulations and simplifications, it can be shown that the current at the output of the balanced mixer for the in-phase and quadrature-phase components are

$$\begin{cases} i_I(t) = \sqrt{2}\gamma\cos\left[2\pi\left(\Delta f\right)t + \phi\right] + \eta_I(t), \\ i_Q(t) = \sqrt{2}\gamma\sin\left[2\pi\left(\Delta f\right)t + \phi\right] + \eta_Q(t), \end{cases} \tag{20}$$

where subscripts $(\cdot)_I$ and $(\cdot)_Q$ denote the in-phase and quadrature-phase components, respectively. Additionally,

$$\begin{cases} \eta_I(t) = \eta_{sn,I}(t) + \eta_{f,I}(t), \\ \eta_Q(t) = \eta_{sn,Q}(t) + \eta_{f,Q}(t). \end{cases} \tag{21}$$

In Eq. (21), we have ignored the effect of RIN and DC noise since they appear at the common mode of the ideally modeled balanced mixers and are filtered out. In practice, due to reflections from optical surfaces in the system, there is a DC term that appears in the differential mode. We have assumed ideal optical surfaces so that reflections can be ignored.

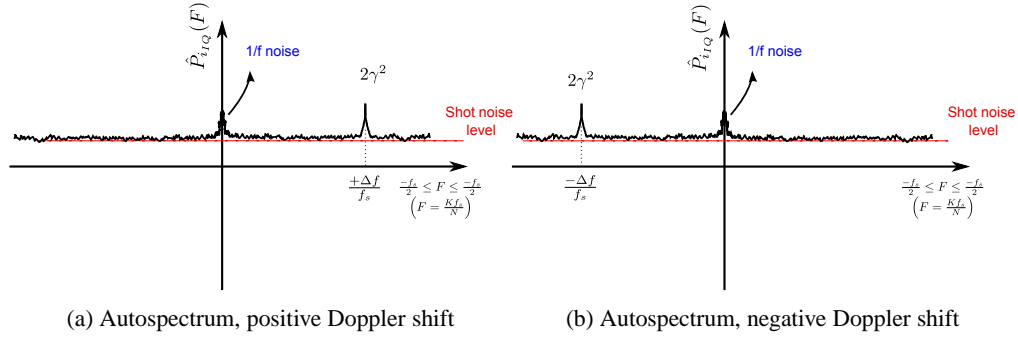(a) Autospectrum, positive Doppler shift   (b) Autospectrum, negative Doppler shift

Fig. 5: Examples of the estimated PSD associated with the baseband signal. (a) The spectra when the radial direction of travel associated with the target is positive. (b) Because the radial direction of travel is away from the telescope, a negative Doppler shift is measured.

The signal pair in Eq. (20) can be combined to make a complex valued signal such that,

$$i_{IQ}(t) = \sqrt{2}\gamma \cos\left(2\pi\Delta f t + \phi\right) + \eta_I(t) + j\left[\sqrt{2}\gamma \sin\left(2\pi\Delta f t + \phi\right) + \eta_Q(t)\right], \qquad (22)$$

where $j = \sqrt{-1}$. Moreover, it can be shown that

$$\begin{cases} P_{i_{IQ}}(\Omega) = 2\gamma^2 \delta(\Omega - \Delta\Omega) + P_{\eta_I}(\Omega) + P_{\eta_Q}(\Omega), \\ \hat{P}_{i_{IQ}}(K) = P_{i_{IQ}}(\Omega_K) + \eta_{est}(K), \end{cases} \qquad (23)$$

and [29]

$$\text{SENR}_{i_{IQ}} = \sqrt{M}\text{SNR}_{i_{IQ}} = \frac{\sqrt{M}\alpha^2 R_D(1-\varepsilon)p}{E}. \qquad (24)$$

Fig. 5(a)-5(b) show examples of the PSD associated with Eq. (23). As can be seen, the PSDs are not symmetric. Also, when compared to the PSDs in Fig. 2(a)-2(b), they are free from RIN and DC noise, thanks to the balanced mixer.

Although the shot noise exhibits a flat spectrum, it is usually shaped due to the presence of filters and electronic components. As a result, to extract the Doppler information it is necessary to whiten the noise [36]. Among other things, noise whitening is a signal processing intensive algorithm and adds to the uncertainty of radial velocity estimation. The image-reject architecture makes the noise whitening redundant due to the availability of two signal observations with independent noise sources. As a result, by performing a cross-spectral analysis between the in-phase and quadrature-phase components we have shown that the signal information, including the direction of travel, is contained in the imaginary part of the result. Thus,

$$\Im\left[P_{i_I i_Q}(\Omega)\right] = \frac{1}{2}\gamma^2\left[\delta(\Omega + \Delta\Omega) - \delta(\Omega - \Delta\Omega)\right], \qquad (25)$$

where

$$P_{i_I i_Q}(\Omega) = \mathscr{F}\left(\mathbb{E}\left[I_I(\Omega)\overline{I_Q(\Omega)}\right]\right), \qquad (26)$$

and $\Im\left[\cdot\right]$ represents the imaginary component. Furthermore,

$$\hat{P}_{i_I i_Q}(K) = \frac{f_s}{M}\sum_{m=0}^{M-1} I_I(K)\overline{I_Q(K)} = P_{i_I i_Q}(\Omega_K) + \eta_{\text{est,IQ}}(K), \qquad (27)$$

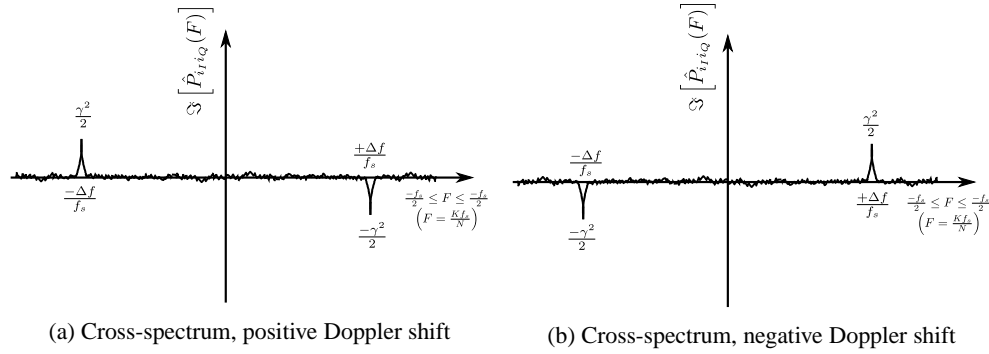(a) Cross-spectrum, positive Doppler shift   (b) Cross-spectrum, negative Doppler shift

Fig. 6: Examples of the estimated cross-spectra of the in-phase and quadrature-phase signal components in baseband. (a) Positive Doppler shift. (b) Negative Doppler shift.

where, similar to Eq. (14), $\eta_{\text{est,IQ}}$ is a zero-mean Gaussian random variable with $\sigma^2_{\eta_{\text{est,IQ}}}$. Moreover, following [29] it can be shown that

$$\text{SENR}_{i_I i_Q} = \frac{\sqrt{2M}\alpha^2 R_D(1-\varepsilon)p}{2E}. \qquad (28)$$

One of the main advantages of the cross-spectral analysis is elimination of uncorrelated noise sources including the shot-noise. Elimination of background noise simplifies the estimation algorithms (including background noise whitening) to extract the Doppler information. It also reduces the number of frequency bins by a factor of 2, which essentially translates into a more efficient storage of spectral data. Moreover, due to the elimination of 1/f noise and DC noise around zero-frequency component, a better estimate of the radial velocities close to zero can be performed. The experimental results, carried out for the measurement of the vertical component of the wind, support the above mentioned claim and will be published in a future paper. This is in contrast to other available system implementations, such as the heterodyne receiver with IF sampling employing an AOM, where the system suffers from added noise by the additional active component (that is, the AOM) and non-ideal filters such as notch filters. Despite its many advantages, the cross-spectral approach suffers from an inherent SENR loss, viz., $\frac{\sqrt{2}}{2}$, [29] that becomes evident when comparing Eq. (24) and Eq. (28).

4. Experimental results

An all-fiber prototype of the proposed architecture in this paper has been built and tested on hard and diffuse targets (atmospheric aerosols). The measurement results for hard and diffused targets, as presented in this section, are solely meant for proof of concept. A detailed analysis of the measurements and how they compare to measurements done by a reference instrument (such as a sonic anemometer) is well beyond the scope of this paper and will be provided in a future paper.

The system follows the schematic illustrated in Fig. 7. An integrated MO and EDFA configuration generates a fiber coupled Gaussian beam at the wavelength of 1565 nm. The maximum output power is around 1.35 W. The output is split by an optical tap into two signals: LO and transmit signals. The splitting ratio is 99/1; that is, 99% of the laser power is directed towards the telescope (via the optical circulator) while 1% of the power is fed into an optical attenuator for fine-tuning of the LO power. For optimal coherent detection the LO power should be large enough so that the photo detectors are in shot-noise limited operation mode. However, it is imperative to make sure the detectors are not operating in saturation mode. The return signal from
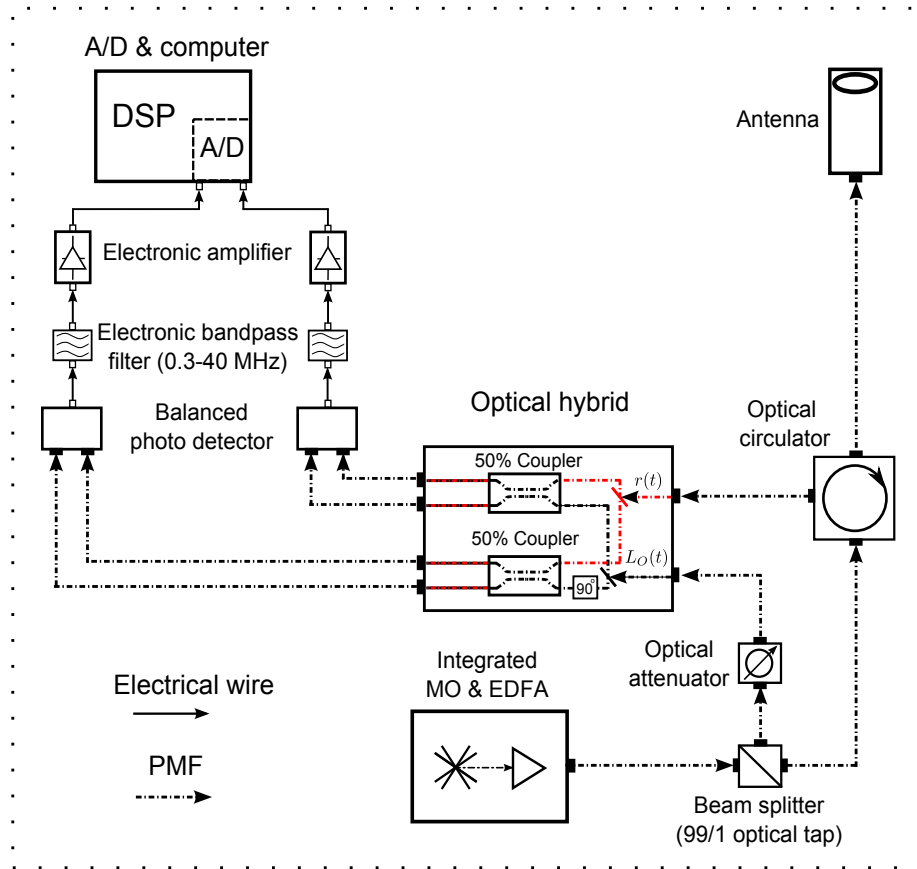
Fig. 7: The schematic of the system set-up. All optical fibers are Panda polarization maintaining fibers. Also, all the optical components in this system are polarization maintaining and fiber coupled. Except the optical antenna (telescope), all the components are commercially available.

the target is collected by the telescope and fed into the optical circulator. Eventually, the signal is passed by the optical circulator to the optical hybrid. The optical hybrid collects the return signal as well as the LO and produces the necessary in-phase and quadrature components in balanced pairs at the output. The results are fed into the balanced photo detectors. After detection, the electrical signal from the the balanced photo detectors are filtered and amplified before being converted into digital signals. The result is processed by the computer where the Doppler information can be extracted. We used an integrated A/D card and National Instrument (NI) computer. Fig. 8 shows a photo of the system set-up in the lab environment.

For measurements on a hard target, a rotating disk was used as the primary target in the lab. Due to strong reflective behavior of the disk the transmit signal power of the laser was adjusted to 70 mW. The target was 5 meters away from the telescope. The laser beam was focused at the distance of 2 meters from the telescope output lens. Table 1 lists the system parameters for the measurement campaigns. As Fig. 9 shows, a wide-band Doppler frequency shift is measured. The wide-band characteristic is due to the transmit signal spot size on the surface of the rotating disk; the rotational speed of the disk varies as a function of the distance from the center of the disk. The narrow dip around zero frequency is due to the high-pass filter. It is evident that despite the presence of the high-pass filter a strong DC component still exists. Furthermore, it
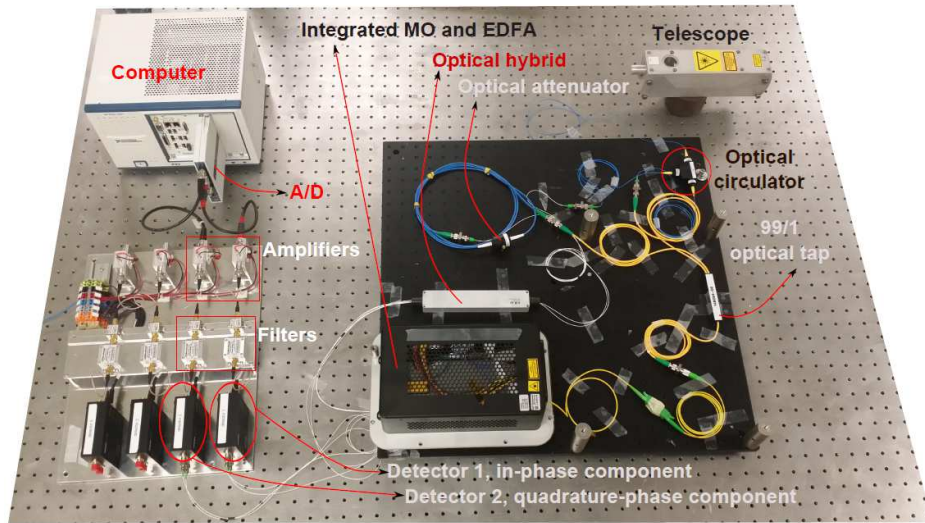
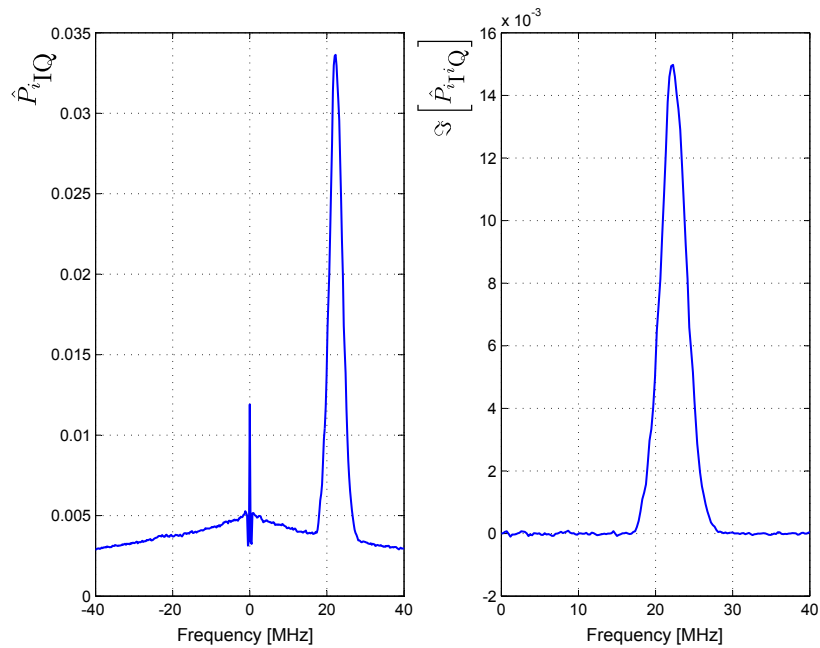Fig. 8: The system set-up in the laboratory environment.

Fig. 9: The measurement on a moving hard target, i.e., a spinning disk. The leftmost plot illustrates the autospectrum of the complex signal, while the rightmost one refers to the one-sided cross-spectra between the in-phase and quadrature-phase signal components. Please note that single-sided cross-spectrum (the right-most plot) represents the left side of the spectrum in Figs. 6(a)-6(b), as it contains all the relevant information for the measurement of radial velocity as well as direction.
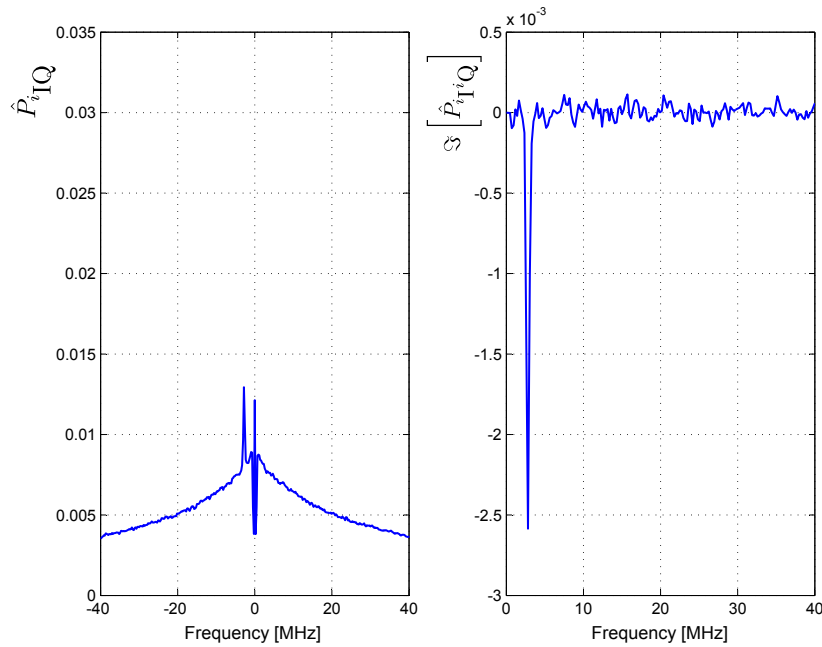
Fig. 10: The atmospheric measurement using the full output power of the laser. The measurement spectra is associated with the vertical component of the wind. The leftmost plot illustrates the autospectrum of the complex signal, while the rightmost one refers to the one-sided cross-spectra between the in-phase and quadrature-phase signal components. Please note that single-sided cross-spectrum (the right-most plot) represents the left side of the spectrum in Figs. 6(a)-6(b), as it contains all the relevant information for the measurement of radial velocity as well as direction.

can be seen that the autospectrum, the leftmost plot in Fig. 9, exhibits a colored (filtered) Gaussian noise as expected across its frequency span. The filtering effect might become significant due to environmental dependency of the electronic components. As a result, for the autospectrum shown in the left-most plot in Fig. 9, noise whitening needs to be carried out before an accurate radial speed can be estimated. The rightmost plot in Fig. 9 illustrates the one-sided cross-spectral analysis, as a result of which the uncorrelated noise sources, e.g., shot noise, 1/f noise, and DC noise due to reflections from the telescope, are suppressed. Besides, due to a relatively flat background spectrum, noise whitening is not required in this case. Thus, radial velocity estimation is not only easier but also more accurate than the autospectral analysis for the majority of scenarios.

Table 1: Experimental system parameters

Campaign	p_t [W]	BW [MHz]	f_s [MHz]	N	M	Aperture size [inches]
Hard target	70×10^{-3}	40	120	512	4000	2
Diffuse target	1.1	40	120	512	4000	2

For atmospheric measurements, the full output power of the integrated MO and EDFA was

used. Due to losses in the system (e.g., fiber connectors) the maximum output power to the telescope was 1.1 W. Fig. 10 illustrates the atmospheric measurement. For this campaign the telescope was pointing upward. As a result, the vertical component of the wind was measured. We know from experience that measuring the vertical component accurately is a challenge due to the presence of the Doppler signal in the vicinity of the DC component (i.e., zero frequency). As seen in the leftmost plot in Fig. 10, the signal strength is much lower and the Doppler shift is closer to zero. Accurate estimation of radial velocity in this case also requires additional signal processing and filtering. However, by utilizing the cross-spectral analysis, the majority of noise sources are suppressed and a rather flat spectra is achieved. It is evident that the benefits of cross-spectral analysis are more emphasized for weaker Doppler signals and lower radial velocity speeds, where dilution with various noise sources around zero frequency is more severe. As we will show in a future paper, however, the merits of the cross-spectral technique become questionable once the Doppler spectrum crosses the zero frequency, where the signal contains both negative and positive Doppler shifts close to zero.

5. Conclusion

By analyzing a promising new approach, an all-fiber image-reject architecture, for signal detection in fiber CDLs, we have shown that a more robust system implementation can be realized. The robustness is partly the result of using passive components, as opposed to alternative system implementations such as heterodyne receivers that use active components, and partly attributable to a new approach in signal processing algorithm made available due to the presence of in-phase and quadrature-phase signal components. Despite its simplicity, the signal processing algorithm, the cross-spectral analysis, improves the accuracy of Doppler shift estimation by eliminating the estimation inaccuracies often introduced by noise whitening procedure, as well as suppressing the major extraneous noise present in the auto-spectral counter-part. Additionally, the presented system profits from a lower memory requirement for the storage of the estimated spectra. The new approach benefits from an all-fiber technology available in fiber optic communications and is easy to implement.